nanomaterials

MDPI

Article

High-Performance Layered CaV_4O_9-MXene Composite Cathodes for Aqueous Zinc Ion Batteries

Luan Fang †, Li Lin †, Zhuomei Wu, Tianhao Xu *, Xuxu Wang, Limin Chang * and Ping Nie

Key Laboratory of Preparation and Applications of Environmental Friendly Material of the Ministry of Education & College of Chemistry, Jilin Normal University, Changchun 130103, China

* Correspondence: 1808016@jlnu.edu.cn (T.X.); aaaa2139@163.com (L.C.)

† These authors contributed equally to this work.

Abstract: Due to their reliability, affordability and high safety, rechargeable aqueous zinc ion batteries (ZIBs) have garnered a lot of attention. Nevertheless, undesirable long-term cycle performance and the inadequate energy density of cathode materials impede the development of ZIBs. Herein, we report a layered CaV_4O_9-MXene ($Ti_3C_2T_x$) composite assembled using CaV_4O_9 nanosheets on $Ti_3C_2T_x$ and investigate its electrochemical performance as a new cathode for ZIBs, where CaV_4O_9 nanosheets attached on the surface of MXene and interlamination create a layered 2D structure, efficiently improving the electrical conductivity of CaV_4O_9 and avoiding the stacking of MXene nanosheets. The structure also enables fast ion and electron transport. Further discussion is conducted on the effects of adding MXene in various amounts on the morphology and electrochemical properties. The composite shows an improved reversible capacity of 274.3 mA h g^{-1} at 0.1 A g^{-1}, superior rate capabilities at 7 A g^{-1}, and a high specific capacity of 107.6 mA h g^{-1} can be delivered after 2000 cycles at a current density of 1 A g^{-1}. The improvement of the electrochemical performance is due to its unique layered structure, high electrical conductivity, and pseudo capacitance behavior.

Keywords: aqueous; zinc ion batteries; vanadium-based cathode; CaV_4O_9; MXene

Citation: Fang, L.; Lin, L.; Wu, Z.; Xu, T.; Wang, X.; Chang, L.; Nie, P. High-Performance Layered CaV_4O_9-MXene Composite Cathodes for Aqueous Zinc Ion Batteries. *Nanomaterials* **2023**, *13*, 1536. https://doi.org/10.3390/nano13091536

Academic Editor: Henrich Frielinghaus

Received: 27 March 2023
Revised: 19 April 2023
Accepted: 25 April 2023
Published: 3 May 2023

1. Introduction

The energy crisis and environmental pollution make the development of large-scale energy storage systems imminent. Lithium-ion batteries (LIBs) dominate the energy storage field of 3C electronics and the electric vehicle industry [1–4]. Nevertheless, the limited resources of lithium, safety, and high cost dramatically hinder the future sustainability of lithium-ion batteries [5–7]. Recently, aqueous zinc ion batteries (ZIBs) with lower cost, higher security, high efficiency, and ultra-high theory capacity (820 mAh g^{-1}) have attracted increasing attention [8–10]. Yet, achieving high performance aqueous ZIBs with long-term life cycles and high energy density remains a challenge owing to the low electrical conductivity and structural instability of conventional cathode materials [11–15]. Currently, the widely reported cathodes for ZIBs are mainly based on manganese- or vanadium-based oxides, Prussian blue analogs, spinel-structured oxides, and organic materials [5,16–19]. Among those materials, vanadium-based materials show promising because of their tremendous natural richness, multiple valence states, and unique layered structure.

Although vanadium-based materials have made great progress in the intercalation/deintercalation of Zn^{2+}, such materials often suffer from slow diffusion kinetics, irreversible phase transitions, and even structural collapse [20,21]. One of the most effective strategies is the introduction of metal ions such as $M_xV_2O_5{\cdot}nH_2O$ (M = Zn, Ca, Mg). Metal ions in vanadium oxides can enhance the structural stability of the host material, and thus improve the cyclic performance [22,23]. Calcium vanadate (CaV_4O_9, CVO), having a typical lamellar structure in which $[V_4O_9]_n^{2n-}$ sheets consist of a VO_5 square pyramid with shared vertices, shows higher conductivity and specific surface area [20,24–26]. The strength of the V–O

bond is large, can effectively mitigate structural stress change induced by the ion insertion process, and enhance the electrochemical performance of the material. Therefore, CaV_4O_9 is widely used in lithium-ion/sodium-ion batteries. Wu et al. applied CaV_4O_9 as an anode material in lithium-ion batteries [27]; the electrode showed both a high capacity of more than 600 mAh g^{-1} with a safe average discharge potential of about 0.8 V and near-zero volume change characteristics. Xu et al. reported CaV_4O_9 nanowires in sodium-ion batteries [28], and the prepared electrodes delivered high reversible capacity, excellent cycling, and multiplicity performance.

However, the utilization of CaV_4O_9 in zinc ion batteries has rarely been reported. Recently, Du et al. prepared CaV_4O_9/CNTs composite film as the cathode for ZIBs using a consecutive spray printing technique [29]. Ex situ XRD and XPS analysis results demonstrated that the generation of amorphous $V_2O_5 \cdot nH_2O$ during charging, which can provide more ion channels, speeds up charge transfer at the electrode/electrolyte interface. Huang et al. reported an electrochemically induced in situ transformation method to synthesize oxygen-deficient navajoite ($V_5O_{12-x} \cdot 6H_2O$, HVO_d) covered by gypsum ($CaSO_4 \cdot 2H_2O$, GP) layers using CaV_4O_9 as the pristine cathode material. GP facilitates the desolvation of hydrogenated zinc ions through its hydrophilic surface and constrained tunneling [30]. Wu et al. prepared novel hydrated vanadate ($CaV_8O_{20} \cdot 3H_2O$) nanoribbons with graphene as the cathode material for aqueous zinc ion batteries [31]. Ca^{2+} and crystal water as columns enhance the stability of the framework and reduce electrostatic interactions with Zn^{2+}. However, calcium vanadate materials tend to aggregate, showing unsatisfactory cycling stability, low specific capacity (<430 mA h g^{-1}), and their charge storage capacity is much lower than the theoretical capacity of V_2O_5 (585 mA h g^{-1}). To address these issues, compositing conductive material alleviates the volume expansion. As an attractive 2D layered metal carbide/nitride, MXenes have been considered as ideal conductive materials for developing composite electrodes with high-rates due to their unique 2D structure, abundant surface functional groups, high electrical conductivity, and good hydrophilicity [32–34].

Herein, we report the reasonable design of the hierarchical assembled CaV_4O_9-MXene ($Ti_3C_2T_x$) layered composite via a solvothermal method. CaV_4O_9 nanosheets are homogeneously loaded onto the interlayer and surface of MXene, forming a unique layered structure. The morphology can improve the conductivity of the nanocomposites. Furthermore, the strong interaction between grown CaV_4O_9 nanosheets and MXene substrates promotes fast ion insertion/extraction of kinetics and structure stability. Investigations are also conducted into how different amounts of MXene affected the zinc ion storage performance. The pseudocapacitive behavior of CaV_4O_9-$Ti_3C_2T_x$ is further analyzed, playing an essential role in the specific capacity contribution. Due to the benefits of the unique structural characteristics, CaV_4O_9-MXene-0.1 exhibits an enhanced specific capacity of 274.3 mAh g^{-1} at 0.1 A g^{-1}, superior rate capabilities, and long cycling stability, a high specific capacity of 107.6 mAh g^{-1} can be delivered after 2000 cycles at a current density of 1 A g^{-1}.

2. Experimental Methods

2.1. Materials Synthesis

2.1.1. Synthesis of $Ti_3C_2T_x$ MXene

Firstly, 2 g of Ti_3AlC_2 MAX powder was placed in a plastic beaker containing 20 mL of HF (49 wt%), stirred at ambient temperature for 24 h to etch the Al element in the MAX, then the sample was washed with distilled water to pH = 7 and dried in vacuum at 60 °C for 12 h to collect $Ti_3C_2T_x$ MXene powder.

2.1.2. Synthesis of CaV_4O_9-MXene

1 mmol of $Ca(OH)_2$ was added to a mixture of 10 mL glycerol and 10 mL water, 2 mmol V_2O_5 was dispersed in 10 mL of deionized water, then 5 mL H_2O_2 solution was slowly added. Stirring the two solutions separately for 1 h, afterwards it was stirred for 2 h after mixing; finally, MXene powder was added and stirred for another 2 h. The mixture was placed in a 50 mL polytetrafluoroethylene kettle encapsulated in a stainless-steel reactor

and kept at 200 °C for 48 h. After solvothermal reaction, the CaV_4O_9-MXene material was obtained using suction filtration, repeated cleaning with distilled water and ethanol, and the material was dried in vacuum for 12 h. For comparison, the samples with different amounts of MXene, including 0.1 g, 0.2 g, 0.3 g, were prepared, and the obtained samples were labeled as CaV_4O_9-MXene-0.1, CaV_4O_9-MXene-0.2, and CaV_4O_9-MXene-0.3, respectively.

2.2. Characterizations

The prepared products were morphologically analyzed using field emission scanning electronic microscopy (FESEM, JSM-7800F) and transmission electronic microscopy (TEM, JEM-2100, JEOL, Tokyo, Japan). XRD pattern was performed with a powder X-ray diffraction system (XRD, Rigaku d/max PC2500, Tokyo, Japan) with Cu Kα in a range from 5° to 90°. Nitrogen adsorption/desorption isotherms were determined with an Isorb-HP2 analyzer (Quantachrome Instruments, Boynton Beach, FL, USA) at 77 K with liquid nitrogen. X-ray photoelectron spectrometry (XPS) was measured on a Thermo Scientific (Waltham, MA, USA) ESCALAB 250Xi spectrometer.

2.3. Electrochemical Measurements

To prepare the CaV_4O_9-MXene cathode, the electrochemical active material (CaV_4O_9-MXene) was mixed with ethynyl black and polyphenylene fluoride (PVDF) in N-methyl pyrrolidone in a ratio of 8:1:1 by weight, then the slurry was coated on titanium foil polished with sandpaper, while zinc foil and a glass fiber membrane (GF/D) were applied as the anode and separator, respectively. Deoxygenated 3M Zn $(CF_3SO_3)_2$ was used as the electrolyte. Subsequently, the cathode was dried in vacuum under 60 °C for 12 h. CR2032 cells were fabricated using as-prepared electrodes in air. The electrochemical properties of the cells were evaluated using a LAND battery test system (CT2001A), including specific capacity, rate performance, and long-term cycling stability. Cyclic voltammetry (CV) measurements were performed on a CHI 760E electrochemical workstation. Contact angle test was performed on a JC 2000D1 contact Angle tester.

3. Results and Discussion

3.1. Structure Characterization

Figure 1a depicts the preparation process of CaV_4O_9-MXene composite. Firstly, MXene was synthesized via a hydrogen fluoride solution etching Al atom from a MAX phase. CaV_4O_9 nanosheets homogeneously anchored on MXene surface were obtained using a simple solvothermal strategy. We prepared three samples (CaV_4O_9-MXene-0.1, CaV_4O_9-MXene-0.2, and CaV_4O_9-MXene-0.3) with different MXene contents based on the mass of MXene used (0.1 g, 0.2 g, and 0.3 g). Figures 1b–d and S1 displays scan electron microscope (SEM) images of MXene and CaV_4O_9-MXene materials. As can be seen from Figure 1c, CaV_4O_9 nanosheets grew uniformly on the MXene surface and were able to preserve the layer structure of MXene; the morphology can enlarge the layer intervals of MXene and increase the surface area and sites for ion storage. In addition, CaV_4O_9 consists of numerous interleaved ultra-thin nanosheets forming a spherical flower structure, which may be due to the absence of MXene substrate. In contrast, composites with a higher concentration of MXene exhibited a stacked layered structure and full coating (Figure S1a–d).

The morphology of CaV_4O_9-MXene-0.1 was investigated using high-resolution transmission electron microscopy (HRTEM). As shown in Figure 1e–g, it appears that the presence of ultrathin CaV_4O_9 nanosheets uniformly anchored on $Ti_3C_2T_x$ layers. The crystalline lattice of CaV_4O_9-MXene-0.1 can be clearly seen in Figure 1f**.** The crystal lattice distance was 0.24 nm, indexed to the (310) crystal plane of CaV_4O_9 [26]. Energy dispersive X-ray spectroscopy (EDS) element mapping further revealed the uniform distribution of calcium, carbon, fluorine, titanium, vanadium, and oxygen elements in CaV_4O_9-MXene-0.1 material (Figure 1g).

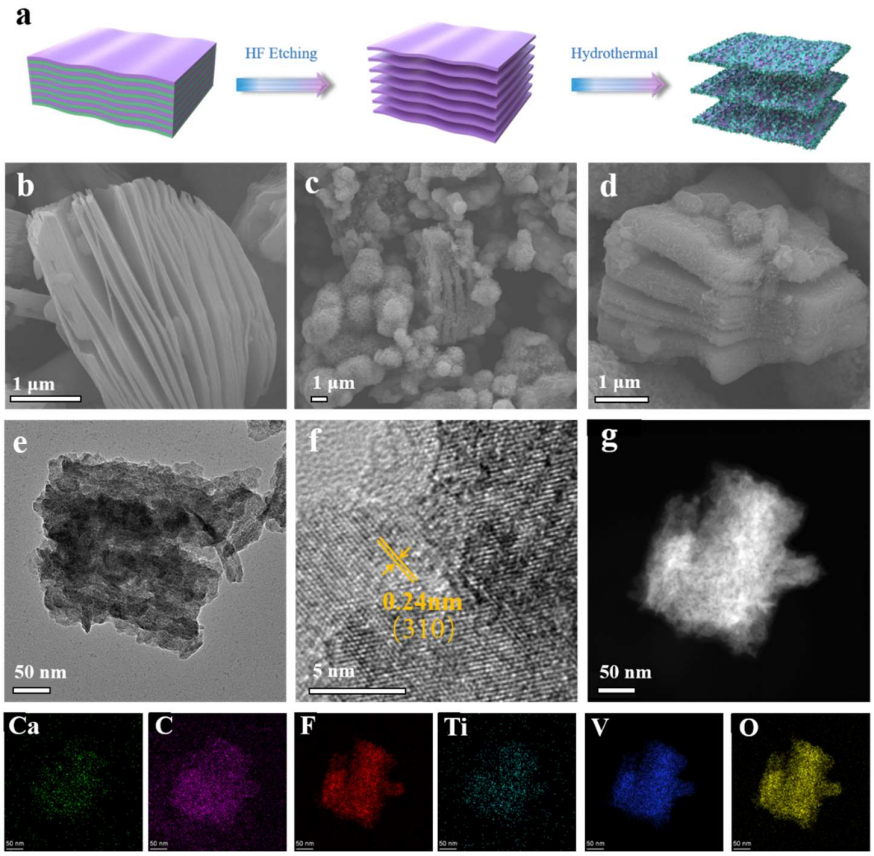

Figure 1. (**a**) Schematic illustration showing the synthesis process of CaV_4O_9-MXene composite, (**b**) SEM images of MXene, (**c**,**d**) SEM images of CaV_4O_9-MXene-0.1, (**e**,**f**) HRTEM images of CaV_4O_9-MXene-0.1, and (**g**) STEM image and EDS elemental mappings of Ca, C, F, Ti, V, and O of the CaV_4O_9-MXene-0.1.

To explore the microstructure of the CaV_4O_9-MXene cathode material synthesized under different amounts of MXene, XRD patterns were recorded (Figure 2a). From the XRD patterns, we found that the characteristic peaks of composites appeared at 29.8°, 33.7°, 43.5°, and 48.8°, respectively, and no impurity was detected, showing that CaV_4O_9 is a purified phase [35]. The composite showed weak MXene diffraction peaks compared with pure MXene, which may be due to the low MXene content and the coating of CaV_4O_9 nanosheets on the MXene surface. X-ray photoelectron spectroscopy (XPS) was used to analyze the surface chemical properties and chemical states of CaV_4O_9-MXene-0.1. Based on the full spectrum of CaV_4O_9-MXene-0.1, peaks at 346.8 eV, 517.4 eV, and 531.0 eV correspond to Ca 2p, V 2p, and O 1s, respectively (Figure S2). As shown in Figure 2b, the Ca 2p spectrum showed two types of bands at 347.5 eV and 350.8 eV [36]. In the high-resolution V 2p spectrum (Figure 2c), CaV_4O_9-MXene-0.1 showed the characteristic peak attributed to V^{4+} at 515.7 and 531.4 eV, and the dominant V^{5+} signal at 517.2 and 529.7 eV [37]. The surface area of CaV_4O_9-Mxene-0.1 was measured using the N_2 adsorption/desorption curves (Figure 2d). The results showed that the specific surface area of the composite was 20.315 $m^2\ g^{-1}$ due to the uniform coating of CaV_4O_9 nanoflakes on the surface of MXene. The adsorption and desorption curves showed that the CaV_4O_9-MXene-0.1 composite had H_3 hysteresis loops in the type IV isotherm [6,38], indicating mesoporous properties of the composites.

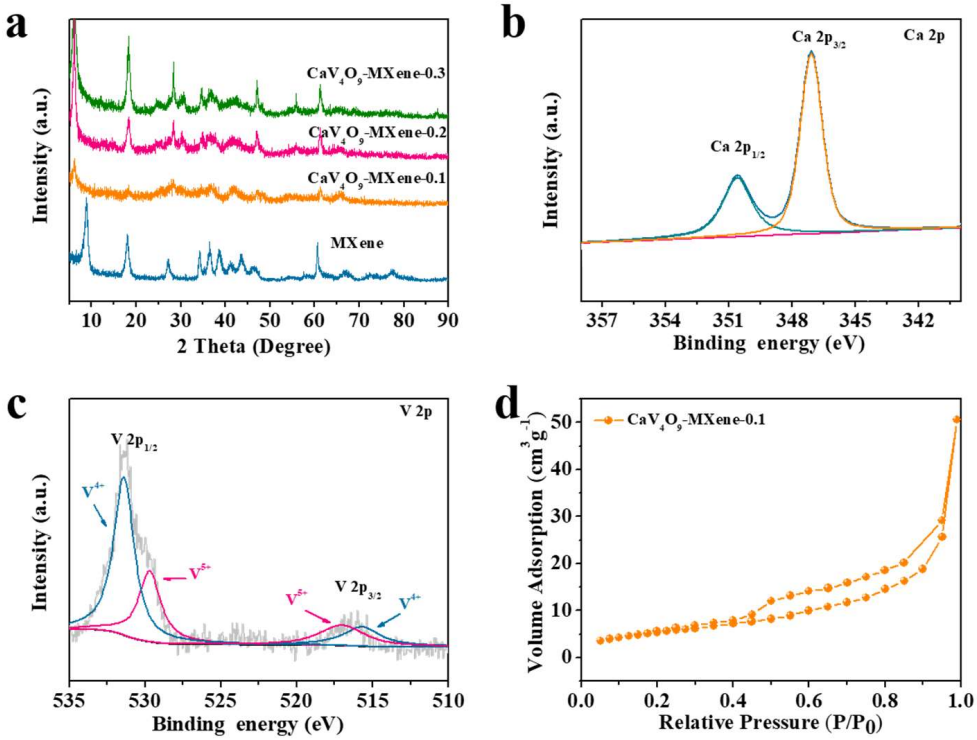

Figure 2. (**a**) XRD patterns of CaV_4O_9-MXene samples, (**b**) XPS spectra of CaV_4O_9-MXene-0.1 composite: Ca 2p region, (**c**) V 2p region, (**d**) nitrogen adsorption/desorption isotherms of CaV_4O_9-MXene-0.1.

3.2. Electrochemical Performance

To identify the distinctive structural benefits of CaV_4O_9-MXene material, electrochemical tests were carried out. Figure S3 shows the galvanostatic charge–discharge (GCD) curve of MXene at a current density of 0.1 A g^{-1}. As can be seen, the stable discharge capacity was only 39 mAh g^{-1}, and after compositing with CaV_4O_9, a higher specific capacity was obtained (Figures 3a and S4). By comparing the composites with different proportions, CaV_4O_9-MXene-0.1 achieved a higher specific discharge capacity of 274.3 mAh g^{-1} after 10 cycles, which means that the composite may be helpful to improve the zinc storage capacity of CaV_4O_9-MXene material. Notably, the low Coulombic efficiencies of the first cycle correspond to electrolyte decomposition and SEI film formation [39]. The rate performance of the MXene and CaV_4O_9-MXene cathode is compared in Figure 3b at different current densities from 0.1 to 2 A g^{-1}. Taking CaV_4O_9-MXene-0.1 as an example, the discharge capacities of 271.6 mAh g^{-1}, 267.2 mAh g^{-1}, 254.2 mAh g^{-1}, 232.1 mAh g^{-1}, and 207.5 mAh g^{-1} can be achieved at current densities of 0.1, 0.2, 0.5, 1, and 2 A g^{-1}, respectively. While the current recovered back to 0.1 A g^{-1}, the reversible capacity was covered to 260.1 mAh g^{-1}, corresponding to a capacity retention of 95.8%. Similarly, for CaV_4O_9-MXene-0.2 and CaV_4O_9-MXene-0.3, as the current rate recovered after 50 cycles to 0.1 A g^{-1}, the discharge capacity was 159.6 and 202.6 mAh g^{-1}, respectively. Obviously, compared with pure MXene, the composite material exhibited improved electrochemical properties, among which the performance of CaV_4O_9-MXene-0.1 was the best, in accordance with the results of galvanostatic charge/discharge test.

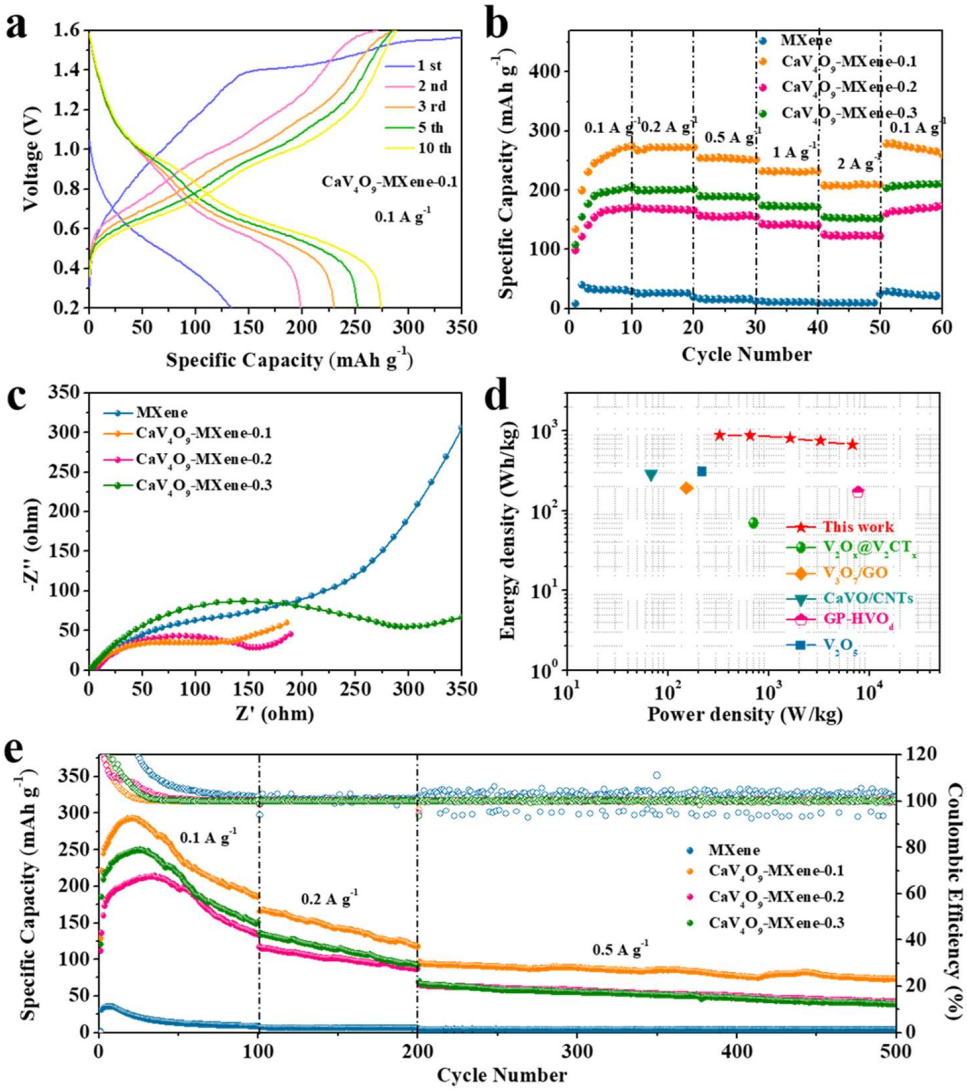

Figure 3. Electrochemical properties of CaV_4O_9-MXene composites as cathodes for AZIB: (**a**) galvanostatic charge/discharge curves of CaV_4O_9-MXene-0.1 at 0.1 A g^{-1} in 0.2–1.6 V, (**b**) rate capability of CaV_4O_9-MXene composite from 0.1 to 2 A g^{-1}, (**c**) EIS of MXene and CaV_4O_9-MXene composites, (**d**) the Ragone plots of CaV_4O_9-MXene compared with other reported cathode materials in aqueous ZIBs, (**e**) cyclic performance of CaV_4O_9-MXene composite at different current densities.

In comparison with pure MXene, all composites displayed improved cycling properties as shown in Figure 3e. When the current density was 0.1 A g^{-1}, the specific discharge capacity of CaV_4O_9-MXene-0.1 remained at 185.1 mA h g^{-1} after 100 cycles. We continued to carry out the cycle performance test at 0.2 A g^{-1}. After 100 cycles, the specific discharge capacity was still 117.4 mA h g^{-1}. When we used a higher current density of 0.5 A g^{-1}, the specific discharge capacity was 73.2 mA h g^{-1} after 300 cycles. This shows that the CaV_4O_9-MXene composite exhibits good stability. The electrolyte ion and electron transport characteristics of MXene and the CaV_4O_9-MXene composite were further analyzed using electrochemical impedance spectroscopy (EIS) (Figure 3c). The semicircle observed in the high frequency area responds to the charge transfer (Rct) impedance at the interface [40]. The *R*ct value of CaV_4O_9-MXene was significantly lower than that of MXene, indicating faster charge transfer in electrochemical reactions. For comparison, CaV_4O_9-MXene-0.1 showed smaller impedance and better conductivity, indicating the faster kinetics characteristics of CaV_4O_9-MXene over MXene. The Ragone plots are shown in Figure 3d; the delivered specific energy and power density of CaV_4O_9-MXene was 888.79 Wh kg^{-1} at 325.56 W kg^{-1}, and 675.93 Wh kg^{-1} at

6759.3 W kg^{-1}, which is superior than other reported cathodes in aqueous ZIBs, such as V_2O_x@V_2CT_x (70 Wh kg^{-1}, 705.6 W kg^{-1}) [34], V_3O_7/GO (191.8 Wh kg^{-1}, 153.4 W kg^{-1}) [41], CaVO/CNTs (290 Wh kg^{-1}, 68 W kg^{-1}) [29], GP-HVO_d (173 Wh kg^{-1}, 7688 W kg^{-1}) [42], and V_2O_5 (310.3 Wh kg^{-1}, 217.8 W kg^{-1}) [43].

To determine the reaction mechanism, cyclic voltammetry (CV) curves were obtained in initial several cycles at a scan rate of 0.05 mV s^{-1} in the voltage range of 0.2–1.6 V. As shown in Figure 4a, the CV curve showed two pairs of distinct redox peaks. The oxidation peaks were located at 0.671 V and 1.001 V, and the reduction peaks were at 0.577 V and 0.94 V, respectively. It is proved that there is a two-step reaction process in the insertion/extraction process of Zn^{2+} [44]. In the following scan, the CV curve had a good degree of coincidence, and the redox peak of CaV_4O_9-MXene-0.1 was almost unchanged, which proves good stability and reversibility. At high current density (Figure 4b), the CaV_4O_9-MXene-0.1 still exhibited an excellent capacity retention. When the current density ranged from 0.1 to 7 to 0.1 A g^{-1}, the CaV_4O_9-MXene-0.1 electrode showed excellent rate performance, and CaV_4O_9-MXene-0.1 provided higher reversible capacities of 246.6, 185.5, 164.1, 137.4, and 130.2 mA h g^{-1} at 0.1, 1, 2, 5, and 7 A g^{-1}, respectively. When the current gradually recovered to 0.1 A g^{-1}, 77.1% of the initial capacity was restored, indicating that MXene can synergistically accelerate kinetics and enhance the rate capability. Figure 4c is the comparison of cycle performance at a current density of 1 A g^{-1}. The specific discharge capacity of CaV_4O_9-MXene-0.1 in the first cycle was 221.6 mA h g^{-1}, which can be stably cycled for 2000 times. The cycling performances of the CaV_4O_9-MXene-0.2 and CaV_4O_9-MXene-0.3 composites showed obvious attenuation, and CaV_4O_9-MXene-0.1 showed the best cycling stability. The rate and cycling performance of CaV_4O_9-MXene were superior to many reported vanadium-based cathodes (Table S1).

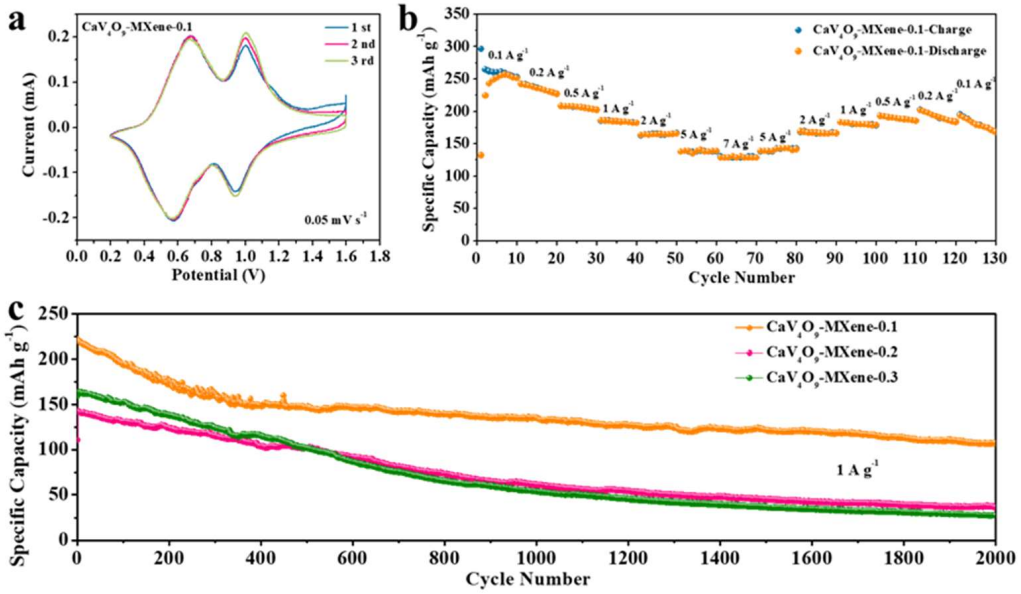

Figure 4. (**a**) Typical CV curves of CaV_4O_9-MXene-0.1 recorded with a scan rate of 0.05 mV s^{-1}, (**b**) rate capability of CaV_4O_9-MXene-0.1 composite from 0.1 to 7 A g^{-1}, (**c**) cyclic performance of CaV_4O_9-MXene composite at 1 A g^{-1}.

3.3. Electrochemical Kinetics

To further reveal the electrochemical kinetics of the zinc ion diffusion process and the contribution of pseudo capacitance behavior of the CaV_4O_9-MXene-0.1 electrode, CV curves in the voltage range of 0.2–1.6 V at different scan rates are provided in Figure 5a. All CV curves showed two pairs of redox peaks with similar shape, which correspond to the voltage plateau of the charge–discharge curves and can be attributed to a two-step reaction

of Zn^{2+} in the CaV_4O_9-MXene lattice. Generally, the relationship between peak current (i) and scan rate (v) can be expressed as:

$$i = av^b \tag{1}$$

$$\log(i) = blog(v) + log(a) \tag{2}$$

where i and v are current and scan rate, and a and b are variable parameters. In Formula (2), the slopes of log (i) and log (v) can be used to calculate the value of b, which can analyze the charge storage mechanism during electrochemical reactions [45]. When the electrode process is controlled by diffusion, the value of b is 0.5, manifesting as the response current proportionating to the square root of the voltage scan rate. When the electrode process is controlled by capacitance, the value of b is one. As shown in b, the b values of peaks P1, P2, P3, and P4 are 0.83, 0.97, 0.88, and 0.73, respectively, demonstrating that the electrode is mainly controlled by the pseudo capacitance and, thus, has a fast zinc storage performance. In addition, the potential-dependent capacitive behavior is identified by the previously reported method:

$$i = k_1 v + k_2 v^{1/2} \tag{3}$$

where k is a constant and the responding current (i) at a given voltage (V) is quantified as $k_1\nu$ (capacitive effect) and $k_2\nu^{1/2}$ (diffusion control behavior) [11]. The equation can be transferred into the format below:

$$i/v^{1/2} = k_1 v^{1/2} + k_2 \tag{4}$$

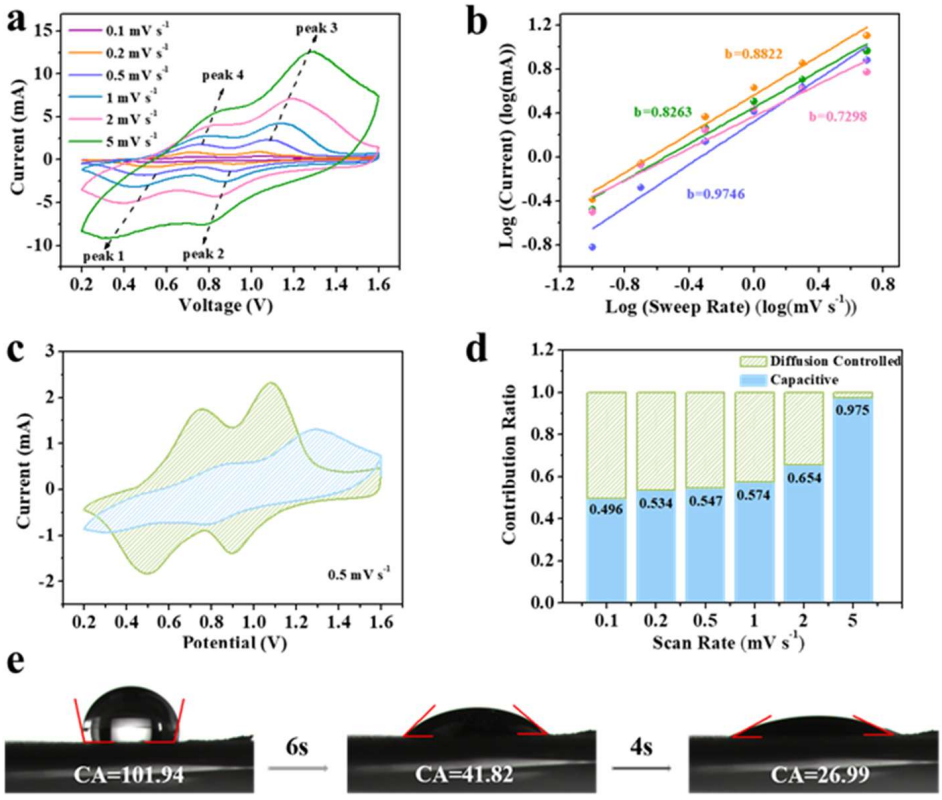

Figure 5. (**a**) CV profiles at various scan rates for CaV_4O_9-Mxene-0.1, (**b**) b values of anode and cathode peak currents determined by fitting log (i) vs. log (ν), (**c**) CV at 0.5 mV s^{-1}, blue shaded area indicating capacitance contribution, (**d**) ratio of the contribution of capacitance and diffusion behavior at different scan rates, (**e**) contact angles of an electrolyte droplet on CaV_4O_9-MXene-0.1 sample.

Therefore, it can be analyzed based on the linear relationship between $i/v^{1/2}$ and $v^{1/2}$. From Figure 5c, the contribution of pseudo capacitance was about 54.7% at a scan speed of 0.5 mV s^{-1}. As shown in Figure 5d, the contribution rate of pseudo capacitance at different scan rates was obtained. When the scan rate was 0.1, 0.2, 0.5, 1, 2, and 5 mV s^{-1}, the contribution was 49.6, 53.4, 54.7, 57.4, 65.4, and 97.5%, respectively. The high pseudo capacitance control is helpful to accelerate the charging and discharging rate. A high percentage of capacitive behavior can bring fast response kinetics of the electrodes, which contributes to its high-rate properties. Furthermore, the contact angle of CaV_4O_9-MXene-0.1 after dropping with 2 μL electrolyte reached 101.94° immediately, and subsequently reduced to 26.99° after 10 s, indicating good wettability (Figure 5e). This facilitated the reduction in resistance and fast Zn^{2+} transfer.

4. Conclusions

In summary, we designed and synthesized a CaV_4O_9-MXene composite through an efficient solvothermal strategy. CaV_4O_9 nanosheets were uniformly anchored on the layer and surface of MXene, which expanded the MXene layer. The expanded specific surface area provided abundant active sites for Zn^{2+} storage, and the addition of MXene enhanced the electrical conductivity. Benefiting from the synergistic effect of enhanced electron/ion transfer and a unique layered structure, the as-obtained CaV_4O_9-MXene exhibited an excellent cycling and rate performance when used as a cathode for AZIBs. Specifically, the CaV_4O_9-MXene-0.1 cathode exhibited a highly reversible capacity of 107.6 mAh g^{-1} after 2000 cycles at a current density of 1 A g^{-1}. It showed good rate performance with a specific capacity of 142.9 mAh g^{-1}, even at a high current density of 7 A g^{-1}. Additionally, it had excellent structural stability, high energy density, and power density (888.79 Wh kg^{-1} at 325.56 W kg^{-1}). This work provides a method for the design of high-performance electrode materials featuring layered MXene and vanadium-based materials, and creates a novel pathway for the application of low-cost ZIBs systems.

Supplementary Materials: The following supporting information can be downloaded at: https://www.mdpi.com/article/10.3390/nano13091536/s1, Figure S1: (a,b) SEM images of CaV_4O_9-MXene-0.2 and CaV_4O_9-MXene-0.3 (c,d); Figure S2: XPS spectrum of the CaV_4O_9-MXene-0.1 composite; Figure S3: Galvanostatic charge/discharge curves of MXene at 0.1 A g^{-1}; Figure S4: (a,b) Galvanostatic charge/discharge curves of CaV_4O_9-MXene-0.2 and CaV_4O_9-MXene-0.3 at 0.1 A g^{-1}, respectively; Table S1: The comparison of the rate and cycling performance of vanadium-based cathodes in aqueous ZIBs. References [46–53] are cited in the supplementary materials.

Author Contributions: Conceptualization, L.F., L.L. and P.N.; methodology, L.F.; software, L.F.; validation, L.F. and L.L.; formal analysis, L.F., L.L. and X.W.; investigation, L.F.; resources, L.F. and L.L.; data curation, L.F. and L.L.; writing—original draft preparation, L.F. and Z.W.; writing—review and editing, L.F., Z.W., T.X. and P.N.; visualization, L.F.; supervision, T.X., L.C. and P.N.; funding acquisition, L.C. All authors have read and agreed to the published version of the manuscript.

Funding: The authors gratefully acknowledge the financial support provided by the Scientific and Technological Developing Project of Jilin Province (20230508046RC, YDZJ202101ZYTS185, YDZJ202201ZYTS372), Jilin Talent Development Funding (2021Y027), and the Research Program on Science and Technology from the Education Department of Jilin Province (JJKH20220439KJ).

Data Availability Statement: The data presented in this study are available on request from the corresponding author.

Conflicts of Interest: The authors declare no conflict of interest.

References

1. Zhang, N.; Chen, X.; Yu, M.; Niu, Z.; Cheng, F.; Chen, J. Materials chemistry for rechargeable zinc-ion batteries. *Chem. Soc. Rev.* **2020**, *49*, 4203–4219. [CrossRef] [PubMed]
2. Melief, C.J.M. Smart delivery of vaccines. *Nat. Mater.* **2018**, *17*, 482–483. [CrossRef] [PubMed]
3. Li, S.; Wang, K.; Zhang, G.; Li, S.; Xu, Y.; Zhang, X.; Zhang, X.; Zheng, S.; Sun, X.; Ma, Y. Fast Charging Anode Materials for Lithium-Ion Batteries: Current Status and Perspectives. *Adv. Funct. Mater.* **2022**, *32*, 2200796. [CrossRef]

4. Wang, Z.; Zhao, H.; Zhou, B.; Li, J.; Qi, Y.; Liang, K.; Zhao, Q.; Ding, Z.; Ren, Y. In Situ Surface Coating and Oxygen Vacancy Dual Strategy Endowing a Li-Rich $Li_{1.2}Mn_{0.55}Ni_{0.11}Co_{0.14}O_2$ Cathode with Superior Lithium Storage Performance. *ACS Appl. Energy Mater.* **2023**, *6*, 387–396. [CrossRef]
5. Li, C.; Jin, S.; Archer, L.A.; Nazar, L.F. Toward practical aqueous zinc-ion batteries for electrochemical energy storage. *Joule* **2022**, *6*, 1733–1738. [CrossRef]
6. Li, X.; Chen, Z.; Yang, Y.; Liang, S.; Lu, B.; Zhou, J. The phosphate cathodes for aqueous zinc-ion batteries. *Inorg. Chem. Front.* **2022**, *9*, 3986–3998. [CrossRef]
7. Zampardi, G.; La Mantia, F. Open challenges and good experimental practices in the research field of aqueous Zn-ion batteries. *Nat. Commun.* **2022**, *13*, 687. [CrossRef]
8. Ming, J.; Guo, J.; Xia, C.; Wang, W.; Alshareef, H.N. Zinc-ion batteries: Materials, mechanisms, and applications. *Mater. Sci. Eng. R Rep.* **2019**, *135*, 58–84. [CrossRef]
9. Zhang, Y.; Wan, F.; Huang, S.; Wang, S.; Niu, Z.; Chen, J. A chemically self-charging aqueous zinc-ion battery. *Nat. Commun.* **2020**, *11*, 2199. [CrossRef]
10. Fang, G.; Zhou, J.; Pan, A.; Liang, S. Recent Advances in Aqueous Zinc-Ion Batteries. *ACS Energy Lett.* **2018**, *3*, 2480–2501. [CrossRef]
11. Cui, H.; Wang, T.; Huang, Z.; Liang, G.; Chen, Z.; Chen, A.; Wang, D.; Yang, Q.; Hong, H.; Fan, J.; et al. High-Voltage Organic Cathodes for Zinc-Ion Batteries through Electron Cloud and Solvation Structure Regulation. *Angew. Chem. Int. Ed.* **2022**, *61*, e202203453. [CrossRef] [PubMed]
12. Zhang, Y.; Tao, L.; Xie, C.; Wang, D.; Zou, Y.; Chen, R.; Wang, Y.; Jia, C.; Wang, S. Defect Engineering on Electrode Materials for Rechargeable Batteries. *Adv. Mater.* **2020**, *32*, e1905923. [CrossRef]
13. Yang, J.; Yin, B.; Sun, Y.; Pan, H.; Sun, W.; Jia, B.; Zhang, S.; Ma, T. Zinc Anode for Mild Aqueous Zinc-Ion Batteries: Challenges, Strategies, and Perspectives. *Nano-Micro Lett.* **2022**, *14*, 42. [CrossRef]
14. Pam, M.E.; Yan, D.; Yu, J.; Fang, D.; Guo, L.; Li, X.L.; Li, T.C.; Lu, X.; Ang, L.K.; Amal, R.; et al. Microstructural Engineering of Cathode Materials for Advanced Zinc-Ion Aqueous Batteries. *Adv. Sci.* **2020**, *8*, 2002722. [CrossRef] [PubMed]
15. Wang, T.; Li, C.; Xie, X.; Lu, B.; He, Z.; Liang, S.; Zhou, J. Anode Materials for Aqueous Zinc Ion Batteries: Mechanisms, Properties, and Perspectives. *ACS Nano* **2020**, *14*, 16321–16347. [CrossRef] [PubMed]
16. Zhang, M.; Liang, R.; Or, T.; Deng, Y.-P.; Yu, A.; Chen, Z. Recent Progress on High-Performance Cathode Materials for Zinc-Ion Batteries. *Small Struct.* **2020**, *2*, 2000064. [CrossRef]
17. Dong, H.; Li, J.; Guo, J.; Lai, F.; Zhao, F.; Jiao, Y.; Brett, D.J.L.; Liu, T.; He, G.; Parkin, I.P. Insights on Flexible Zinc-Ion Batteries from Lab Research to Commercialization. *Adv. Mater.* **2021**, *33*, e2007548. [CrossRef]
18. Wang, X.; Zhang, Z.; Xi, B.; Chen, W.; Jia, Y.; Feng, J.; Xiong, S. Advances and Perspectives of Cathode Storage Chemistry in Aqueous Zinc-Ion Batteries. *ACS Nano* **2021**, *15*, 9244–9272. [CrossRef]
19. Shang, Y.; Kundu, D. A path forward for the translational development of aqueous zinc-ion batteries. *Joule* **2023**, *7*, 244–250. [CrossRef]
20. Wang, L.; Cao, X.; Xu, L.; Chen, J.; Zheng, J. Transformed Akhtenskite MnO_2 from Mn_3O_4 as Cathode for a Rechargeable Aqueous Zinc Ion Battery. *ACS Sustain. Chem. Eng.* **2018**, *6*, 16055–16063. [CrossRef]
21. Ding, Y.; Xue, W.; Chen, K.; Yang, C.; Feng, Q.; Zheng, D.; Xu, W.; Wang, F.; Lu, X. Sodium Ion Pre-Intercalation of delta-MnO_2 Nanosheets for High Energy Density Aqueous Zinc-Ion Batteries. *Nanomaterials* **2023**, *13*, 1075. [CrossRef]
22. Zhao, S.; Tian, G.; Zhang, D.; Wang, Q. Controlled Synthesis of Metal–Organic-Framework-Derived V_2O_5 Nanostructures with Polypyrrole Coating for Zinc-Ion Batteries. *ACS Appl. Nano Mater.* **2023**, *6*, 1849–1858. [CrossRef]
23. Tan, S.; Sang, Z.; Yi, Z.; Guo, J.; Zhang, X.; Li, P.; Si, W.; Liang, J.; Hou, F. Conductive coating, cation-intercalation, and oxygen vacancies co-modified vanadium oxides as high-rate and stable cathodes for aqueous zinc-ion batteries. *EcoMat* **2023**, *5*, e12326. [CrossRef]
24. Guan, H.; Feng, Y. Preparation of ultrathin two-dimensional CaV_4O_9 nanosheets: A new inorganic graphene-like material. *Mater. Lett.* **2014**, *131*, 222–224. [CrossRef]
25. Chen, Y.; Ma, D.; Shen, S.; Deng, P.; Zhao, Z.; Yang, M.; Wang, Y.; Mi, H.; Zhang, P. New insights into high-rate and super-stable aqueous zinc-ion batteries via the design concept of voltage and solvation environment coordinated control. *Energy Stor. Mater.* **2023**, *56*, 600–610. [CrossRef]
26. Li, Z.; Wei, Y.; Liu, Y.; Yan, S.; Wu, M. Dual Strategies of Metal Preintercalation and In Situ Electrochemical Oxidization Operating on MXene for Enhancement of Ion/Electron Transfer and Zinc-Ion Storage Capacity in Aqueous Zinc-Ion Batteries. *Adv. Sci.* **2023**, *10*, e2206860. [CrossRef] [PubMed]
27. Wu, P.; Xu, X.; Wu, Y.; Xu, F.; Wang, X.; Meng, J.; Han, C.; Liu, X.; Zhu, Z.; Mai, L. A Stable CaV_4O_9 Anode Promises Near-Zero Volume Change and High-Capacity Lithium Storage. *Adv. Energy Mater.* **2021**, *11*, 2003612. [CrossRef]
28. Xu, X.; Niu, C.; Duan, M.; Wang, X.; Huang, L.; Wang, J.; Pu, L.; Ren, W.; Shi, C.; Meng, J.; et al. Alkaline earth metal vanadates as sodium-ion battery anodes. *Nat. Commun.* **2017**, *8*, 460. [CrossRef]
29. Du, Y.; Wang, X.; Zhang, Y.; Zhang, H.; Man, J.; Liu, K.; Sun, J. High mass loading CaV_4O_9 microflowers with amorphous phase transformation as cathode for aqueous zinc-ion battery. *Chem. Eng. J.* **2022**, *434*, 134642. [CrossRef]
30. Li, J.; Hong, N.; Luo, N.; Dong, H.; Kang, L.; Peng, Z.; Jia, G.; Chai, G.; Wang, M.; He, G. In-situ electrochemical modification of pre-intercalated vanadium bronze cathodes for aqueous zinc-ion batteries. *Sci. China Mater.* **2022**, *65*, 1165–1175. [CrossRef]

31. Wu, Q.; Li, X.; Fan, H.; Cao, J.; Liu, X.; Wei, M.; Yang, L. Synergistic interlayer and structure engineering construction of layered hydrated vanadates/graphene for stable aqueous zinc-ion batteries. *J. Alloys Compd.* **2023**, *941*, 168936. [CrossRef]
32. Zhu, X.; Cao, Z.; Wang, W.; Li, H.; Dong, J.; Gao, S.; Xu, D.; Li, L.; Shen, J.; Ye, M. Superior-Performance Aqueous Zinc-Ion Batteries Based on the In Situ Growth of MnO_2 Nanosheets on V_2CT_X MXene. *ACS Nano* **2021**, *15*, 2971–2983. [CrossRef]
33. Shi, M.; Wang, B.; Shen, Y.; Jiang, J.; Zhu, W.; Su, Y.; Narayanasamy, M.; Angaiah, S.; Yan, C.; Peng, Q. 3D assembly of MXene-stabilized spinel $ZnMn_2O_4$ for highly durable aqueous zinc-ion batteries. *Chem. Eng. J.* **2020**, *399*, 125627. [CrossRef]
34. Venkatkarthick, R.; Rodthongkum, N.; Zhang, X.; Wang, S.; Pattananuwat, P.; Zhao, Y.; Liu, R.; Qin, J. Vanadium-Based Oxide on Two-Dimensional Vanadium Carbide MXene ($V_2Ox@V_2CTx$) as Cathode for Rechargeable Aqueous Zinc-Ion Batteries. *ACS Appl. Energy Mater.* **2020**, *3*, 4677–4689. [CrossRef]
35. Narayanasamy, M.; Kirubasankar, B.; Shi, M.; Velayutham, S.; Wang, B.; Angaiah, S.; Yan, C. Morphology restrained growth of V(2)O(5) by the oxidation of V-MXenes as a fast diffusion controlled cathode material for aqueous zinc ion batteries. *Chem. Comm.* **2020**, *56*, 6412–6415. [CrossRef] [PubMed]
36. Zhu, K.; Wu, T.; Huang, K. A High Capacity Bilayer Cathode for Aqueous Zn-Ion Batteries. *ACS Nano* **2019**, *13*, 14447–14458. [CrossRef]
37. Wu, F.; Wang, Y.; Dai, X.; Meng, S.; Zheng, D.; Yin, R.; Liu, W.; Shi, W.; Cao, X. Toward Ultralong Lifespan Aqueous Zinc-Ion Batteries via Sulfur-Defect Vanadium Tetrasulfide Cathode. *ACS Appl. Energy Mater.* **2023**, *6*, 2680–2686. [CrossRef]
38. Liu, M.; Chang, L.; Wang, J.; Li, J.; Jiang, J.; Pang, G.; Wang, H.; Nie, P.; Zhao, C.; Xu, T.; et al. Hierarchical N-doped carbon nanosheets submicrospheres enable superior electrochemical properties for potassium ion capacitors. *J. Power Sources* **2020**, *469*, 228415. [CrossRef]
39. Huang, Z.; Chen, A.; Mo, F.; Liang, G.; Li, X.; Yang, Q.; Guo, Y.; Chen, Z.; Li, Q.; Dong, B.; et al. Phosphorene as Cathode Material for High-Voltage, Anti-Self-Discharge Zinc Ion Hybrid Capacitors. *Adv. Energy Mater.* **2020**, *10*, 2001024. [CrossRef]
40. Wang, Z.; Song, Y.; Wang, J.; Lin, Y.; Meng, J.; Cui, W.; Liu, X.X. Vanadium Oxides with Amorphous-Crystalline Heterointerface Network for Aqueous Zinc-Ion Batteries. *Angew. Chem. Int. Ed.* **2023**, *62*, e202216290. [CrossRef]
41. Tian, C.-Y.; Li, Y.-D.; Du, D.-N.; Zhang, Y.-S.; Zhang, B.-M.; Zhang, D.-T.; Kong, L.-B.; Liu, M.-C. Hydrothermal reaction induced phase transition of vanadium oxide towards high-performance zinc ion batteries cathode. *Ionics* **2021**, *27*, 4793–4800. [CrossRef]
42. Huang, J.; Liang, H.; Tang, Y.; Lu, B.; Zhou, J.; Liang, S. In Situ Induced Coordination between a "Desiccant" Interphase and Oxygen-Deficient Navajoite towards Highly Efficient Zinc Ion Storage. *Adv. Energy Mater.* **2022**, *12*, 2201434. [CrossRef]
43. Li, X.; Li, M.; Yang, Q.; Liang, G.; Huang, Z.; Ma, L.; Wang, D.; Mo, F.; Dong, B.; Huang, Q.; et al. In Situ Electrochemical Synthesis of MXenes without Acid/Alkali Usage in/for an Aqueous Zinc Ion Battery. *Adv. Energy Mater.* **2020**, *10*, 2001791. [CrossRef]
44. Zong, Q.; Wu, Y.; Liu, C.; Wang, Q.; Zhuang, Y.; Wang, J.; Tao, D.; Zhang, Q.; Cao, G. Tailoring layered transition metal compounds for high-performance aqueous zinc-ion batteries. *Energy Stor. Mater.* **2022**, *52*, 250–283. [CrossRef]
45. Li, S.; Liu, Y.; Zhao, X.; Shen, Q.; Zhao, W.; Tan, Q.; Zhang, N.; Li, P.; Jiao, L.; Qu, X. Sandwich-Like Heterostructures of MoS_2 /Graphene with Enlarged Interlayer Spacing and Enhanced Hydrophilicity as High-Performance Cathodes for Aqueous Zinc-Ion Batteries. *Adv. Mater.* **2021**, *33*, e2007480. [CrossRef] [PubMed]
46. Jing, P.; Wei, W.; Luo, W.; Li, X.; Xu, F.; Li, H.; Wei, M.; Yu, D.; Zhu, Q.; Liu, G. In-situ XRD study of the structure and electrochemical performance of V_2O_5 nanosheets in aqueous zinc ion batteries. *Inorg. Chem. Commun.* **2020**, *117*, 107953. [CrossRef]
47. He, P.; Yan, M.; Zhang, G.; Sun, R.; Chen, L.; An, Q.; Mai, L. Layered VS_2 Nanosheet-Based Aqueous Zn Ion Battery Cathode. *Adv. Energy Mater.* **2017**, *7*, 1601920. [CrossRef]
48. Xu, G.; Zhang, Y.; Gong, Z.; Lu, T.; Pan, L. Three-dimensional hydrated vanadium pentoxide/MXene composite for high-rate zinc-ion batteries. *J. Colloid Interface Sci.* **2021**, *593*, 417–423. [CrossRef]
49. Xia, C.; Guo, J.; Li, P.; Zhang, X.; Alshareef, H.N. Highly Stable Aqueous Zinc-Ion Storage Using a Layered Calcium Vanadium Oxide Bronze Cathode. *Angew. Chem. Int. Ed.* **2018**, *57*, 3943–3948. [CrossRef]
50. Yang, G.; Wei, T.; Wang, C. Self-Healing Lamellar Structure Boosts Highly Stable Zinc-Storage Property of Bilayered Vanadium Oxides. *ACS Appl. Mater. Interfaces* **2018**, *10*, 35079–35089. [CrossRef]
51. Hu, P.; Yan, M.; Zhu, T.; Wang, X.; Wei, X.; Li, J.; Zhou, L.; Li, Z.; Chen, L.; Mai, L. Zn/V_2O_5 Aqueous Hybrid-Ion Battery with High Voltage Platform and Long Cycle Life. *ACS Appl. Mater. Interfaces* **2017**, *9*, 42717–42722. [CrossRef] [PubMed]
52. Ming, F.; Liang, H.; Lei, Y.; Kandambeth, S.; Eddaoudi, M.; Alshareef, H.N. Layered $MgxV_2O_5{\cdot}nH_2O$ as Cathode Material for High-Performance Aqueous Zinc Ion Batteries. *ACS Energy Lett.* **2018**, *3*, 2602–2609. [CrossRef]
53. Park, J.-S.; Jo, J.H.; Aniskevich, Y.; Bakavets, A.; Ragoisha, G.; Streltsov, E.; Kim, J.; Myung, S.-T. Open-Structured Vanadium Dioxide as an Intercalation Host for Zn Ions: Investigation by First-Principles Calculation and Experiments. *Chem. Mater.* **2018**, *30*, 6777–6787. [CrossRef]